Available online at www.sciencedirect.com

jmr&t Journal of Materials Research and Technology

journal homepage: www.elsevier.com/locate/jmrt

Original Article

Solidification behavior and microstructural features of the cast and HIPed N-bearing Ti–48Al–2Cr–2Nb intermetallic alloys

Hamid Reza Ghorbani, Ahmad Kermanpur, Ahmad Rezaeian, Fazlollah Sadeghi, Abbas Ahmadi Siahboumi*

Department of Materials Engineering, Isfahan University of Technology, Isfahan, 84156-83111, Iran

ARTICLE INFO

Article history:
Received 22 December 2022
Accepted 15 April 2023
Available online 20 April 2023

Keywords:
Titanium aluminide
Ti–48Al–2Cr–2Nb
Nitrogen
Ti_2AlN precipitates
Solidification
Hot isostatic pressing

ABSTRACT

Effect of N addition (0.5, 1, and 2 at. %) on solidification behavior and microstructural features of the cast and hot isostatically pressed (HIPed) Ti–48Al–2Cr–2Nb (4822) intermetallic alloy was investigated. Alloys were fabricated using vacuum arc re-melting followed by HIPing. The results showed that N addition changes the primary β phase dendrites to α phase. The morphological uniformity of the as-cast microstructures was notably increased by N addition. In addition, N addition beyond its solubility limit led to the formation of primary Ti_2AlN precipitates located within lamellar colonies. A possible mechanism for nucleation of the Ti_2AlN precipitates is proposed. Furthermore, N addition caused much more microstructure stability during HIPing. Although a duplex structure was formed after HIPing in the 4822 alloy, N addition decreased the formation of this structure. Moreover, highly extended network of secondary Ti_2AlN precipitates were formed in almost all of ($\alpha_2+\gamma$) lamellas interfaces in the N-bearing alloys.

1. Introduction

The material properties including stiffness, strength, corrosion and oxidation resistance, and fatigue performance will be deteriorated at high temperatures. Therefore, advanced materials with high strength and light weight are highly demanded in industrial sectors such as automotive, aerospace, and power plants. Titanium aluminide intermetallic alloys have shown excellent properties such as low density, high specific strength, low diffusivity, and high melting point [1–4]. Among various generation of the titanium aluminide alloys, Ti–48Al–2Cr–2Nb (known as 4822) alloy is currently used in airplane engines. Cast blades of the 4822 alloy have been the most commonly used alloy in the GEnx™ engine since 2011 [1]. The 4822 alloy is still lighter and cheaper than the 3rd (high Nb) and 4th (high Ta) generation series. However, the current disadvantages of low room-temperature ductility and toughness should be addressed [2–4]. Various solutions have already been proposed to improve the mechanical properties, such as addition of different alloying elements [5–14] and microstructure refinement [15,16].

* Corresponding author.
E-mail address: ahmad_k@iut.ac.ir (A. Kermanpur).
https://doi.org/10.1016/j.jmrt.2023.04.138

Among the elements, Nitrogen (N) promotes heterogeneous nucleation through the formation of primary Ti_2AlN precipitates, which in turn produces an ultra-high fine microstructure [10,17]. Also, the precipitates significantly maintain the alloy microstructure even after a long time exposing to high temperatures [18]. Furthermore, N is easily accessible and has a reasonable price. Several researchers studied the effects of N addition and formation of the Ti_2AlN precipitates via experimental observations [10,13,17,19,20] and simulation methods [21–28]. They reported that by N addition, one can manage Ti_2AlN precipitates and make Ti_2AlN network [11,29] or generate composites by combining Ti_2AlN and TiN reinforcements or even composites with Ti_2AlN reinforcements with TiN core [30–32]. In addition, by adjusting the cooling rate or adding alloying materials, secondary Ti_2AlN precipitates can be controlled [33]. It was shown that the Ti_2AlN precipitates have various shapes, crystallographic orientation relationships, and atomic structures of TiAl matrix/Ti_2AlN interface [34]. Moreover, the Ti_2AlN precipitates and their atomic interface structures were simulated in several studies [21–28]. In addition, primary Ti_2AlN precipitates formed in the melt and acted as nucleation points; they usually located within lamellar colonies and were mostly larger than secondary Ti_2AlN precipitates. Additionally, secondary Ti_2AlN precipitates were formed at α_2 and γ lamellas interfaces through a solid-state transformation during the heat treatment [35].

Zhang et al. [10] investigated effect of N addition up to 2.5 at.% on the solidification and microstructure of a 3rd generation titanium aluminide alloy (Ti–46Al–8Nb). Results showed that dissolved N acts as an α phase stabilizer and expands the α phase region. Also, the N alloying changes the initial solidified phase from β to α, mainly due to the suppression effect of N against the diffusion of dissolved Al atoms at the solidification front. By an increase in N content, the amount of γ phase was decreased and the amount of α_2 phase was increased [10]. The lamellar spacing has also decreased by increasing N until the formation of the Ti_2AlN precipitates, further N addition increased lamellar spacing, which is related to Al concentration in the matrix [10,12,36]. In another research work, the N addition up to 1 at.% into Ti-48.5Al-1.5Mo alloy showed a decrease in colony size, leading to an increase in crack path which in turn increases the fracture toughness. Also, the existence of coarse nitrides in colonies boundaries were found to induce stress concentration, leading in generating nucleation sites of cracks [37]. Based on the work of Liu et al. [20], dendritic segregation in the Ti_2AlN/4822 composite is less than in the 4822 alloy; also 3 vol.% Ti_2AlN/4822 composite exhibits better compression properties. Liu et al. [17], produced and investigated Ti_2AlN/Ti–48Al–2Cr–2Nb composites with 3 and 4 vol.% Ti_2AlN reinforcements, respectively. A 4 vol.% Ti_2AlN composite exhibited optimum mechanical properties at room temperature (with highest fracture strain and strength) and high temperature (with highest UTS and yield strength in 800 °C), but the highest elevated-temperature elongation was observed in 3 vol.% Ti_2AlN composite [17]. Saeedipour et al. [12,13] studied the effects of N addition up to 2 at.% on the solidification, microstructure and high temperature (850 °C) mechanical properties of Ti–46Al–8Ta alloy using small punch test (SPT). Results showed that N addition changed the solidification path from primary β phase to primary α phase. In addition, maximum load in SPT experiments was increased by N addition up to 1.05 at.% and was decreased by further N addition. Moreover, they reported that N addition resulted in dendrite refinement and reduction or elimination of remained β phase based on N content [12,13]. Recently Tan et al. [38,39] investigated the effects of N addition up to 1.6 at.% on the microstructural and compression properties of Ti–46Al–4Nb–1Mo alloy, once by adding BN compound [38] and another by adding TiN compound [39]. In another work [38], it was shown that by adding B and N, the B2 phase disappeared and both of the Ti_2AlN and TiB phases were formed in the refined microstructure. Amount of both Ti_2AlN and TiB phases was increased by further addition of BN compounds and various forms of TiB were formed by increasing BN compounds. Finally, the compressive strength was improved. The results reported in [39] showed that microstructure morphology changed from columnar dendrites to equiaxed grains by formation of Ti_2AlN phases and also their size was reduced by further N addition. The room-temperature compressive strength increased for the alloy with 1.6 at.% N due to solid solution, Ti_2AlN precipitates and lamellas refinement. Also, for this alloy the peak stress at the high-temperature (900 °C and 1000 °C) compression tests improved due to strengthening effect of Ti_2AlN precipitates.

The 4822 alloy is the most useable titanium aluminide alloy. It is cheaper and lighter than the 3rd and 4th generation of titanium aluminide alloys. However, 4822 alloy needs to be improved to extend its application more than low-pressure turbine blades. Thus, this research aimed to investigate the effects of low amount of N addition up to 2 at.% on the solidification behavior and microstructural features of the alloy at two conditions of casting and HIPing.

2. Materials and methods

Ti sheet (99.28 wt.%), bulk Al (99.77 wt.%), Nb powder (99.07 wt.%), Cr powder (99 wt.%) from Merck™ and TiN powder from Sigma–Aldrich (595,063) were used as raw materials. The Ti–48Al–2Cr–2Nb-xN (x = 0.5, 1 and 2, all numbers in at.%) alloys were fabricated using a vacuum arc remelting (VAR) furnace employing non-consumable tungsten electrode. Hereafter, the alloys are named 4822, 0.5N, 1N, and 2N alloys, respectively.

The surfaces of Ti sheet pieces and Al pieces were ground to remove surface oxides, followed by ultrasonic cleaning in acetone solution. The VAR furnace chamber was cleaned twice for each melt by evacuating to about 10^{-3} mbar and purging with pure Ar gas. It was finally evacuated to about 3×10^{-3} mbar and filled with pure Ar gas to pressure of 500 mbar. In each melting process at first a small amount of pure titanium (as an oxygen absorber) was melted for 30 s. Then the main alloy components were melted based on Table 1, in which electric current intensity and melting time process are shown. In order to reduce Al loss during first and second melts, a piece of the Ti sheet was located on the VAR furnace stage with the Al pieces placed on it, and finally, a piece of the Ti sheet was placed over the Al pieces. In this order, the arc

Table 1 – Melting parameters (electric current intensity and melting time) of different re-melts for the 4822 and N-bearing alloys.

Melt	4822 alloy				N-bearing alloys					
	$I_{melting}$ (A)		$t_{melting}$ (s)		$I_{melting}$ (A)		$t_{melting}$ (s)			
	Button	Powder	Button	Powder[a]	Button	Powder	Reducing I	Button	Powder/ Heating[a]	
1	150–170	15	60	30	150–170	15	–	60	30	Powder
2	150–170	15	60	60	150–170	15	–	60	60	
3	122	–	90	–	313	15	–	60	60	
4	122	–	90	–	313	–	–	120	40	Preheating
5	122	–	90	–	313	–	24	120	40	
6	122	–	90	–	313	–	–	120	40	
7	122	–	120	–	313	–	–	120	40	
8	205	–	120	–	313	–	–	120	40	
9	250	–	60	–	313	–	100	120	40	
10	–	–	–	–	313	–	220[b]	60	40	

[a] This shows time of preheating titanium sheet and powders in 1st to 3rd melts using 15 A electric current intensity, and also shows time of heating and increasing electric current intensity from 15 A up to 313 A in 4th to 10th melts.
[b] More time required for combining two buttons.

would not directly touch the Al pieces in first and second melts. The 4822 samples were melted 9 times, but the N-bearing samples were melted 10 times while electric current intensity and melting time were increased. The samples were upside down in each melt compared to the previous melt. The 8 times of melting (Table 1) were adequate for melting and dissolution of all starting materials in the 4822 alloy; however, few undissolved TiN particles were observed in the 2N alloy after 10 times of melting. Finally, button samples (20 g and 40 g) for all alloys were produced. It should be noted that heat convection during solidification of the samples was managed to avoid formation of shrinkage porosities. All samples were then conducted to hot isostatic pressing (HIP) treatment under Ar atmosphere at the pressure 110 MPa and temperature 1250 °C for 6 h.

Chemical composition of the 4822 alloy was determined using ICP-OES 730-ES Varian, and the N content of the N-bearing alloys was analyzed by TCH test using TCH 600 LECO^{R} instrument. Thermo-Calc ^{R} calculations using TCTI1, TCTI2 and TCTI2.1 databases were carried out for determining phase fraction versus temperature diagrams in alloys. Differential thermal analysis (DTA) measurements were conducted on 4822 and 2N alloys. DTA measurements were completed in heating and cooling cycles with a rate of 10 °C/min from room temperature to 1450 °C under Ar gas atmosphere using a STA504 thermal analyzer. There was not any sign of melting in samples subjected to DTA measurements.

The etchant solution of 600 ml H_2O + 25 ml HNO_3 + 10 ml HF was used. Microstructure of the alloys at center of the buttons was analyzed using optical microscopy (Nikon-EPI-PHOT 300) and scanning electron microscopy (Philips XI30) equipped with energy-dispersive X-ray spectroscopy (EDS). The EDS analysis was based on the standard ASTM E1508 procedure [40]. In addition, Philips X'PERT-MPD with $Cu_{K\alpha}$ was used for phase analyses using COD 2017 and PDF-2 Release 2011 databases and HighScore Plus software (version 3.0.5). High-resolution transmission electron microscopy (TEM) investigations were carried out on the 2N–HIP alloy using a TEM equipped with EDS at 200 keV (JEOL JEM-2100F), and the data were analyzed using Oxford Aztec® v6.0. Samples for TEM observations were prepared via mechanical polishing (to 100 μm thickness), punching out 3 mm disks, thinning using jet-polish a TenuPol-5 (Struers Aps, Ballerup, Denmark) with 600 ml ethanol, 360 ml butyl glycol, and 60 ml perchloric acid solution and final cleaning and thinning with a precision ion polishing system.

3. Results and discussion

3.1. *Chemical composition*

Chemical composition of the base alloy (4822) was determined to be 58.2% Ti, 32.7% Al, 2.9% Cr, 4.2% Nb, 0.1% Fe, and 1.9% other impurities (all in wt.%). However, to be closer to the nominal composition of 4822 alloy, the amount of starting elements especially Al was slightly adjusted. Results of LECO technique measurements showed that the N content of the 0.5N, 1N and 2N alloys was 0.38 ± 0.04%, 0.68 ± 0.06% and 1.67 ± 0.18%, respectively (all in wt.%).

3.2. *As-cast intermetallic alloys*

3.2.1. *Solidification behavior*

Fig. 1 shows the macrostructure of the buttons produced. Fig. 1a shows one of the 4822 alloy buttons (40 g) showing some pores and also columnar pattern macrostructure. N addition led to generating polished, glossy surfaces as well as shrinkage holes and pores, as shown in Fig. 1(b–f). N addition significantly increased shrinkage and pores following solidification, the pores and shrinkage (Fig. 1e) disappeared by changing heat transfer practice during solidification (Fig. 1f). It was observed that the shrinkage and pores were produced in the buttons when the electric arc was suddenly turned off during melting (Fig. 1a and e). It was also observed that the polished glossy surfaces of the N-bearing buttons (Fig. 1(b, d) and Fig. 1f) were related to their fine microstructure and pore-less surface which will be discussed in the following sections.

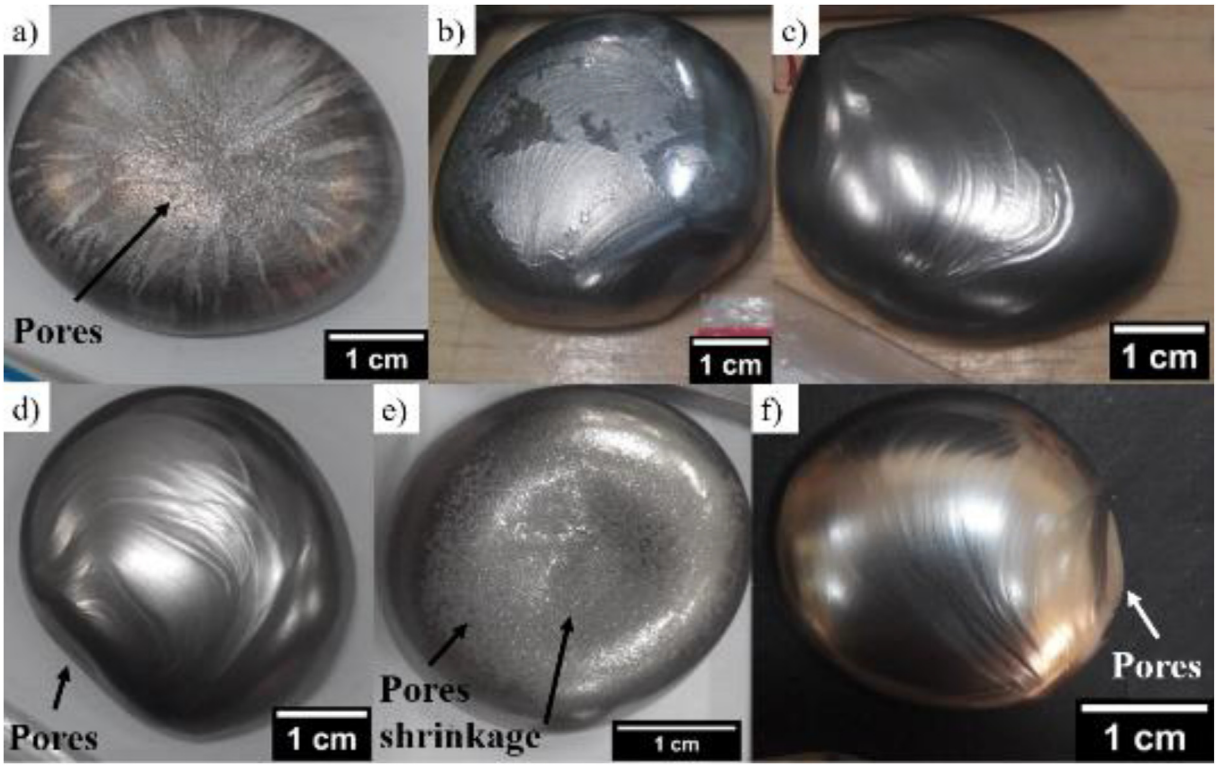

Fig. 1 – Button of samples a) 4822-40 g, b) 0.5N-40 g, c) 1N-40 g, d) 2N-40 g, e) 2N-20 g with shrinkage and f) 2N-20 g without shrinkage.

Final re-melting parameters in all of the N-bearing alloys were precisely chosen in order to reduce the pores and shrinkages.

Fig. 2 shows the SEM micrographs of dendrites observed in the shrinkage pores at or near the top surface of the 4822, 0.5N and 1N samples. The 2N alloy consisted of much finer dendrites which were not clearly observable even in the shrinkage pores (Fig. 2d). Shape and symmetry of solidified dendrites were maintained till end of solidification, but their first inner

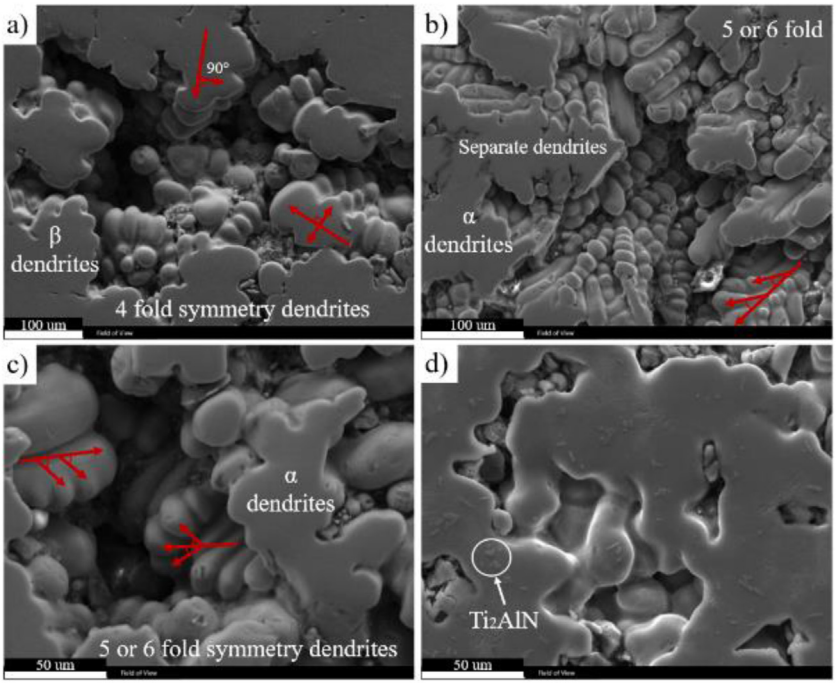

Fig. 2 – SEM micrographs of the dendrites in a) 4822, b) 0.5N, c) 0.5N and d) 1N cast alloys.

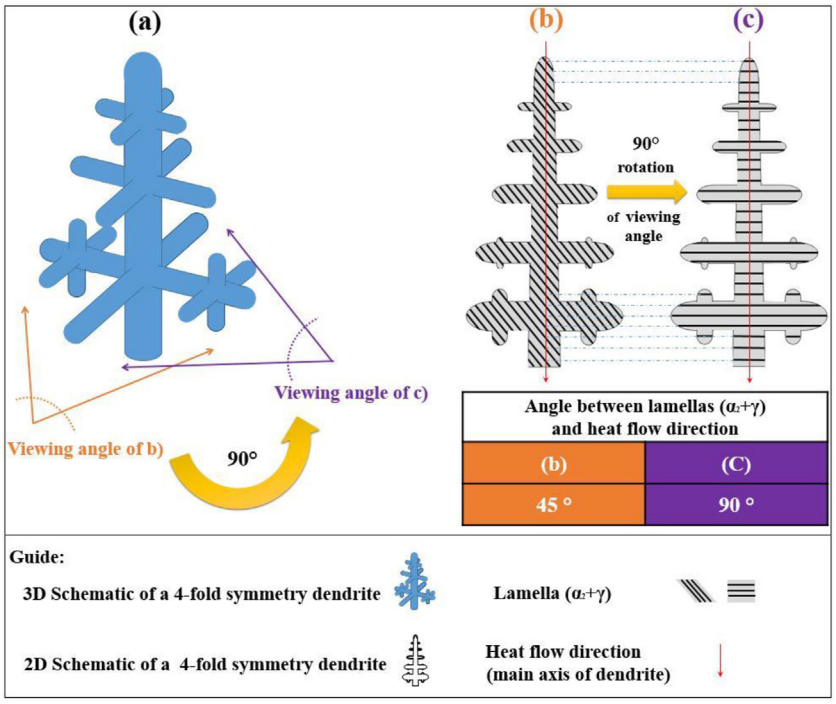

Fig. 3 – A schematic for illustrating effect of dendrite viewing angle on observing the angle between lamellas and heat flow direction.

microstructure and phases were transformed into new ones. Thus it could be possible to identify the first (primary) solidified phase via investigating dendrites forms in shrinkage pores and their microstructure, as reported in other works [12,41–43]. Fig. 2a shows 4-fold symmetry dendrites of the 4822 alloy, which could be β phase. Also, Fig. 2 (b, c) show dendrites in the 0.5N alloy with 5 or 6-fold symmetry to be α phase dendrites. Fig. 2d shows the primary Ti_2AlN precipitates, shrinkage pores and ultra-fine dendrites in the 1N alloy, which are difficult to determine their symmetry. N is α phase stabilizer element in titanium aluminides; so it is expected that the 1N and 2N alloys would also form α phase dendrites based on the effects of N addition on primary dendrites and their symmetry in the 0.5N alloy, Thermo-Calc^R calculations, DTA analysis for the 2N alloy [33], and microstructural observations regarding remained β phase. Therefore, the addition of N altered the solidification behavior from the α phase to the β phase, as has also been noted in other research works [10,12]. According to [43–45], identifying dendrites as β or α phase dendrites based on the orientation of their lamellas ($\alpha_2+\gamma$) to dendrite arms does not produce reliable findings; hence we advise against using this method. They [43,44] proposed 0° and 45° angles between lamellas and dendrite growth direction (heat flow direction) for the primary

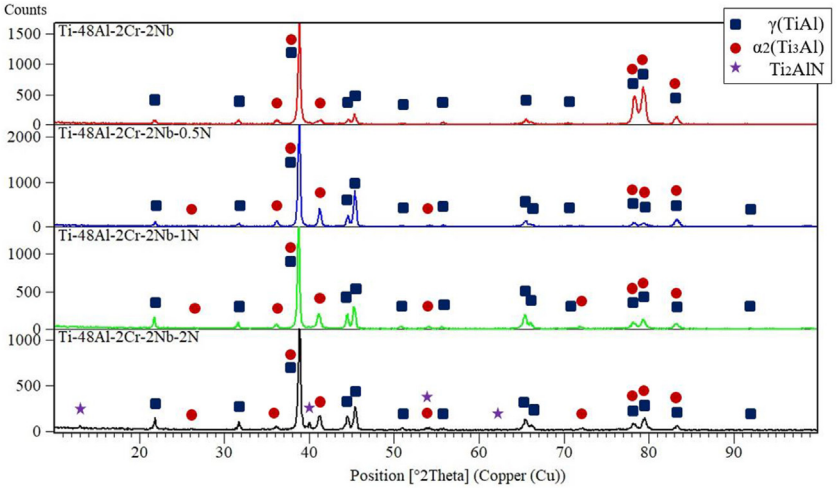

Fig. 4 – XRD patterns of 4822, 0.5N, 1N and 2N as-cast alloys.

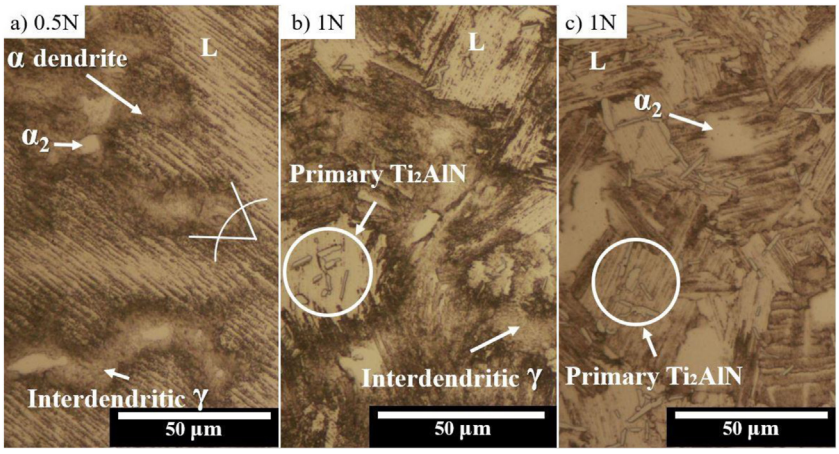

Fig. 5 – Optical micrographs of primary Ti_2AlN precipitates in a) 0.5N, b) 1N and c) 2N cast alloys.

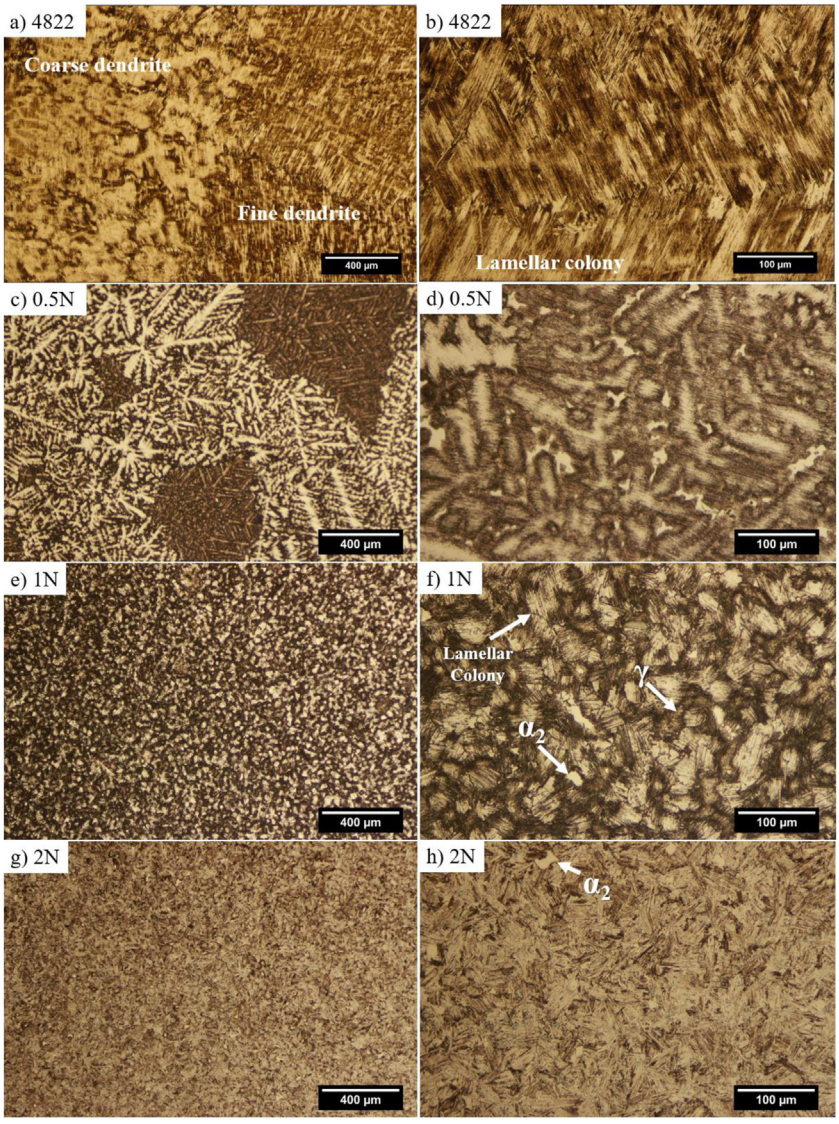

Fig. 6 – Optical micrographs of (a, b) 4822 (c, d) 0.5N (e, f) 1N and (g, h) 2N cast alloys.

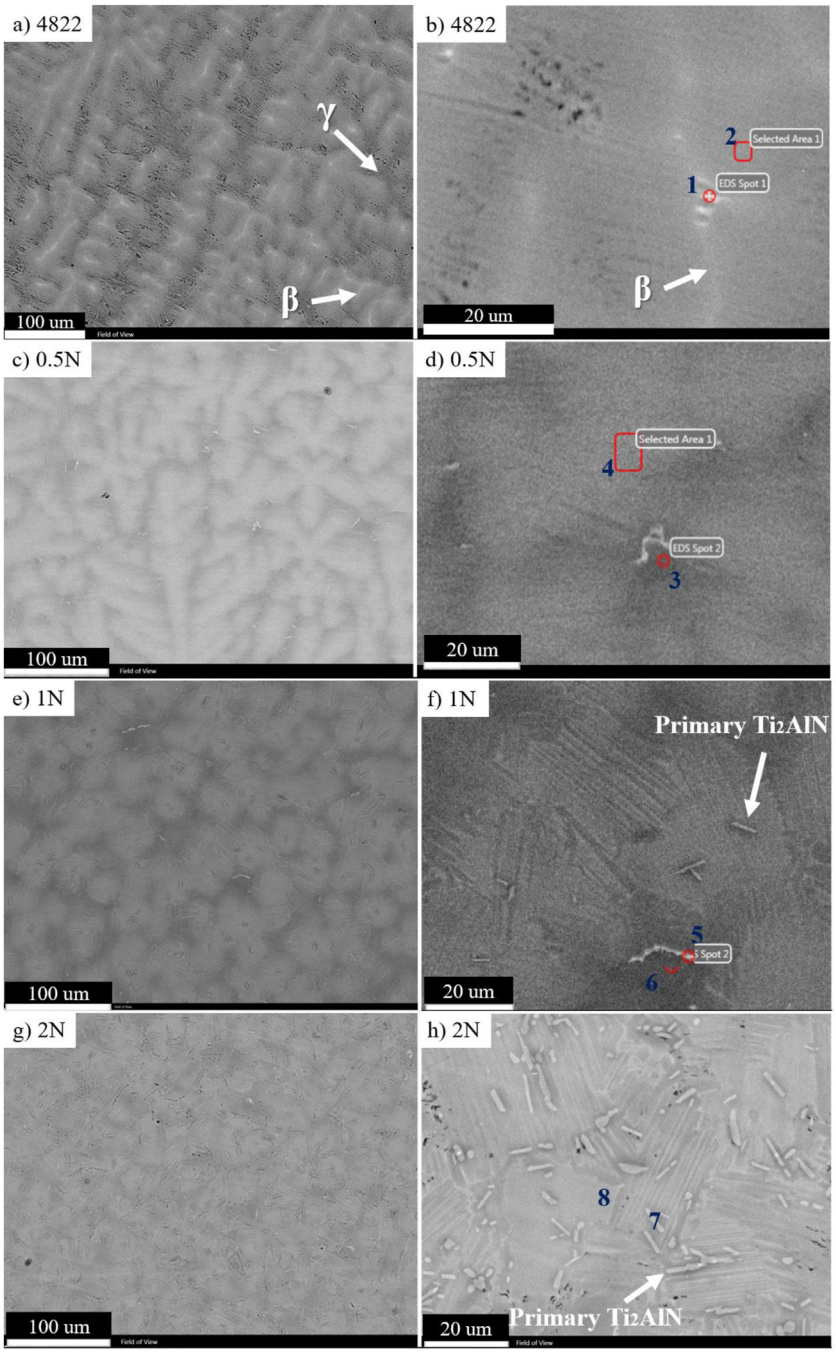

Fig. 7 – SEM micrographs of (a, b) 4822 (c, d) 0.5N (e, f) 1N and (g, h) 2N cast alloys.

β dendrite and 90° for the primary α dendrite; moreover, in other research work [45], the 0°, 45° and 90° were proposed for the primary β dendrite. These hypotheses are based on the idea that the ($\alpha_2+\gamma$) lamellas can be formed in specific orientations from solidified β or α phases, but it is important to note that due to viewing angle, overlapping in microscopic observations is possible. Fig. 3 shows geometry of the dendrites. Fig. 3a shows a three-dimensional schematic of a 4-fold symmetry. Fig. 3(b and c) show two different viewing angles (90° turning) of Fig. 3a in microscopic observations. In Fig. 3b the observable angle between lamellas and growth direction is seen at 45°, but in the same dendrite (Fig. 3c), the observable angle is seen at 90°, by 90° changing the viewer's viewing angle. Thus regardless of dendrite symmetry, there is an overlap in detecting β and α dendrite via the identification method proposed in [43–45]. Therefore, it is impossible to determine the primary α or β dendrites by the angle between lamellas and growth directions. Finally, one can take into account the symmetry of the dendrites and even apply high-tech methods to make their symmetry more obvious in order to distinguish the phases of primary dendrites. For instance, pouring the melt right away while it is still in the

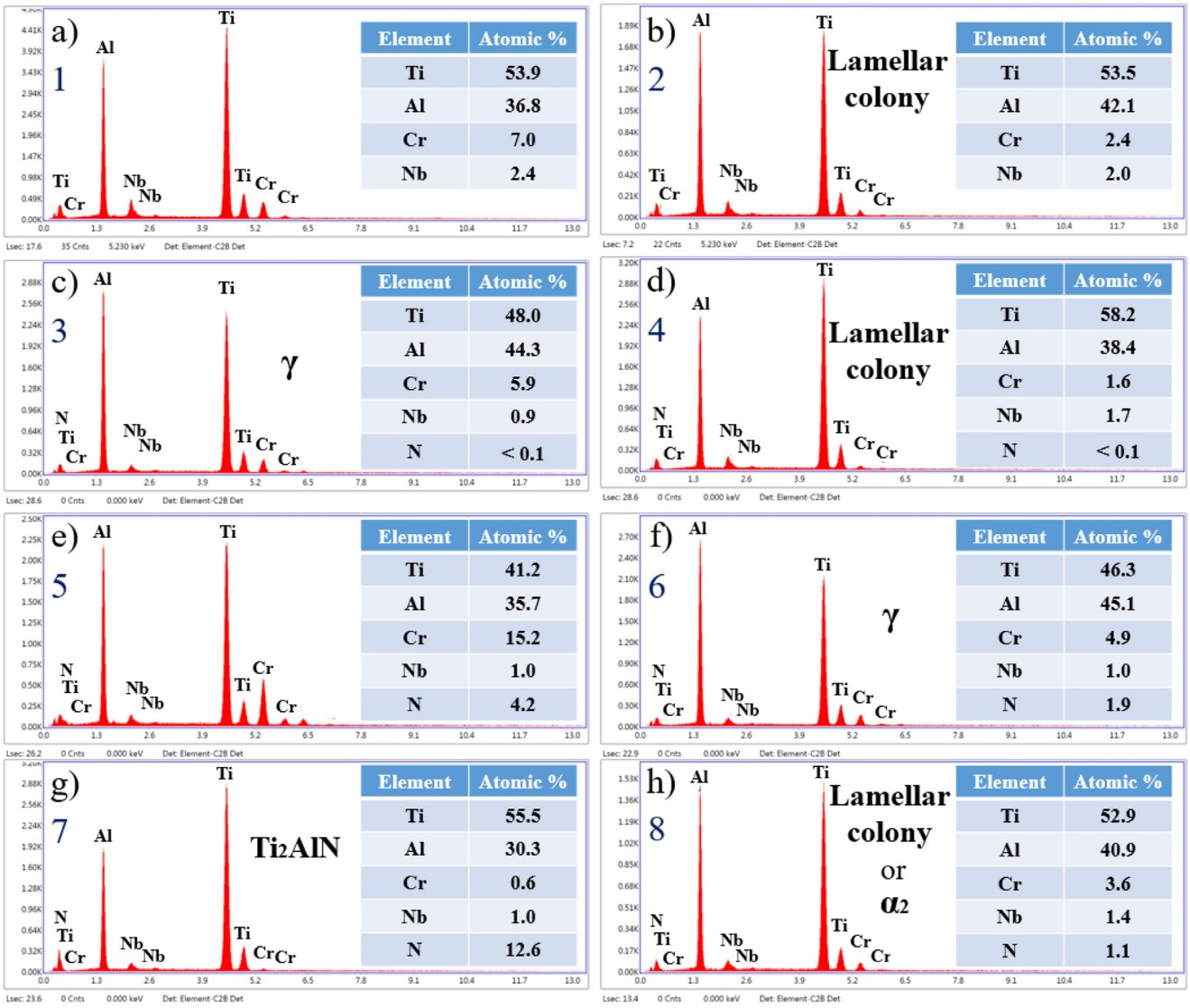

Fig. 8 – Results of the EDS spectra in Fig. 7.

initial stage of solidification or utilizing a sophisticated in-situ sensor to track the solidification front and dendrite development. Other methods for determining the first solidified α or β phase (dendrite) include looking for remained β phase in the dendrite core or interdendritic area in room-temperature microstructures, as well as combining simulation and calculation results with experimental ones using tools like Thermo-Calc^{R} and thermal analysis.

3.2.2. *Phase analysis*

Fig. 4 shows XRD patterns of the as-cast alloys where existence of both α_2 and γ phases were confirmed in all alloys. Also, low amount of primary Ti_2AlN precipitates formed in the 0.5N and 1N alloys resulted in no Ti_2AlN peak detection in the XRD patterns of these alloys, however they were observed in the microstructures using OM and SEM images. As can be seen from Fig. 4, only some peaks corresponding to the Ti_2AlN phase were detected in the 2N alloy, even though their peaks were not strong enough probably due to their low amount, identified according to similar works [17,20]. Fig. 5 shows high magnification optical micrographs of the alloys. As can be seen from Fig. 5a, the primary Ti_2AlN precipitates were relatively low and the dendrite spacing was relatively high. Also, part of a 5-fold symmetry α phase dendrite is shown in Fig. 5a. As the amount of primary Ti_2AlN precipitates was increased (in the 1N and 2N alloys), the dendrites became much finer due to the nucleation effect of these precipitates as shown in Fig. 5(b and c).

3.2.3. *Microstructures*

Figs. 6 and 7 show OM and SEM microstructures of as-cast alloys, respectively. Three types of microstructures from bottom to top of the as-cast alloy can be identified: very fine lamellar colonies (chill zone), coarse lamellar colonies near the bottom of buttons and finally the main microstructure. In the case of the 4822 alloy, the main microstructure contained two types of microstructures due to different cooling rates. It should be emphasized that these microstructural changes

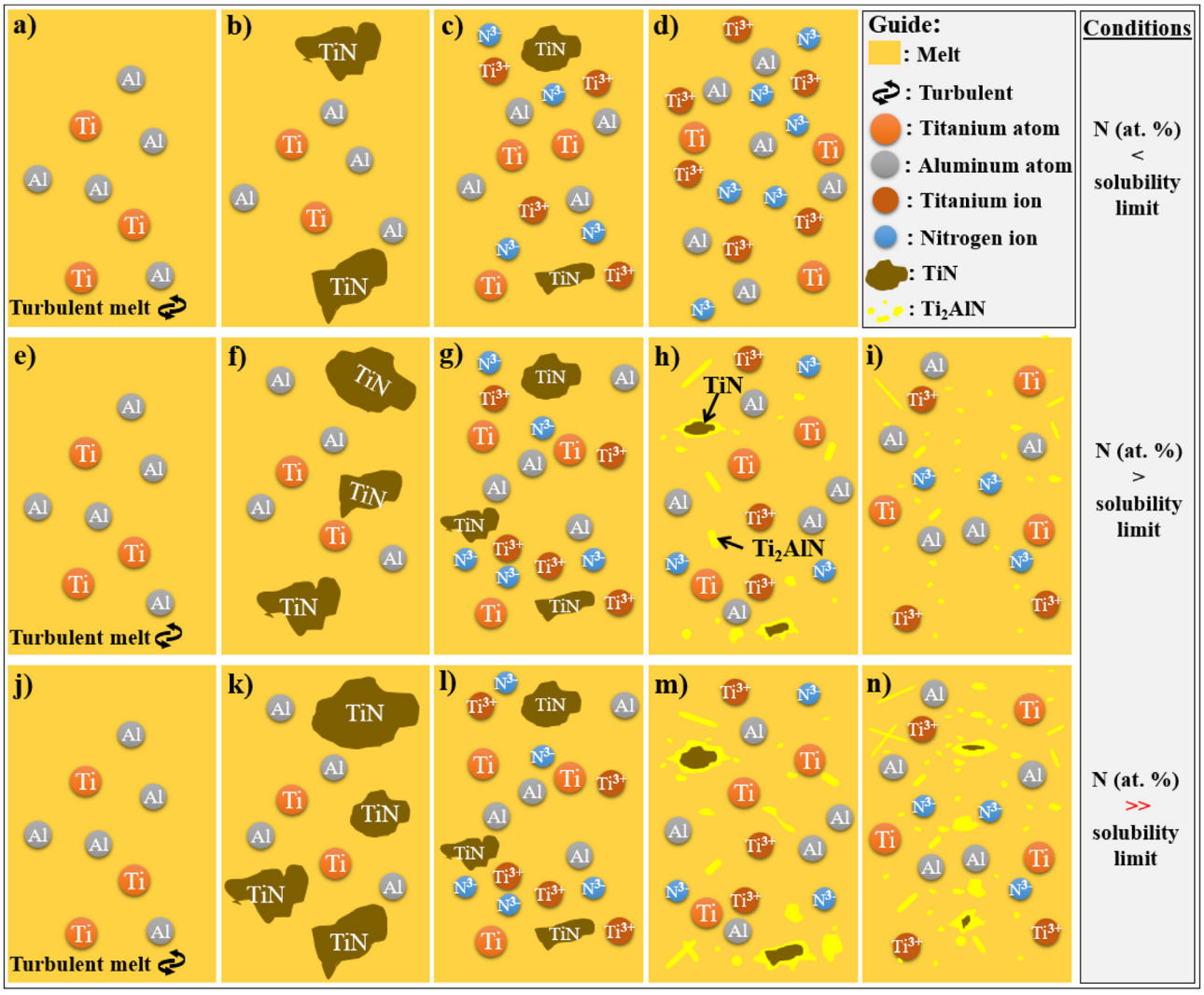

Fig. 9 – A schematic mechanism for nucleation of the primary Ti_2AlN precipitates in alloy with various N content (a–d) less than its solubility limit (e–i) more than its solubility limit and (j–n) much more than its solubility limit.

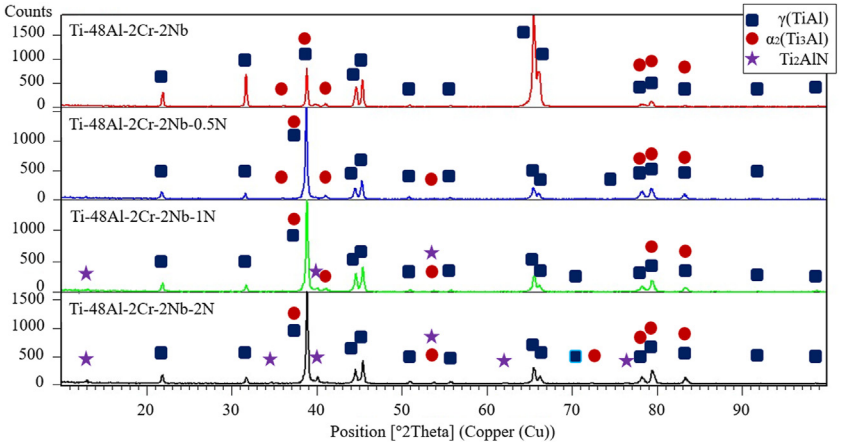

Fig. 10 – XRD patterns of the 4822, 0.5N, 1N, and 2N HIPed alloys.

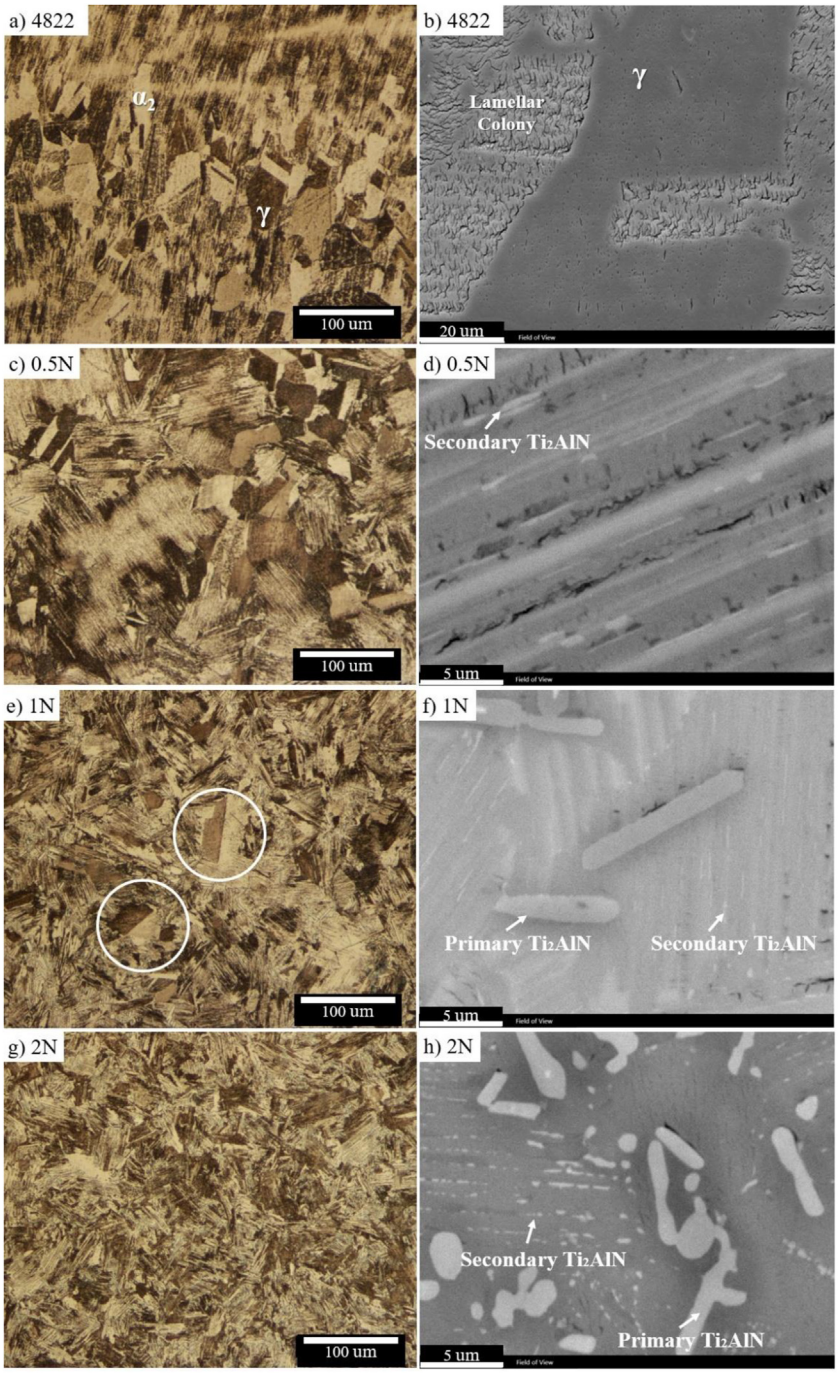

Fig. 11 – (a, c, e, g) Optical and (b, d, f, h) SEM micrographs of the (a, b) 4822 (c, d) 0.5N (e, f) 1N, and (g, h) 2N HIPed alloys.

following melting in the VAR furnace is not due to the changes in chemical compositions but is because of the different solidification conditions within the sample. Since bottom of the buttons were in contact with the water-cooled copper, formation of a chill zone is expected, however, it was not observed in vertical cross section of all alloys. Furthermore, microstructure of bottom of the 2N alloy button contains chill zone microstructure with very fine lamellar colonies with primary Ti_2AlN precipitates. Second type of microstructure (i.e. coarse lamellar colonies) was seen in the 4822 alloy as shown in Fig. 6a, but N-bearing alloys showed equiaxed lamellar colonies with rare primary Ti_2AlN precipitates. The main microstructure of the as-cast alloys for different N contents can be described below.

Alloy 4822: coarse and fine columnar fully lamellar dendritic microstructure
Alloy 0.5N: coarse and fine equiaxed fully lamellar dendritic microstructure showing low area of primary Ti_2AlN precipitates

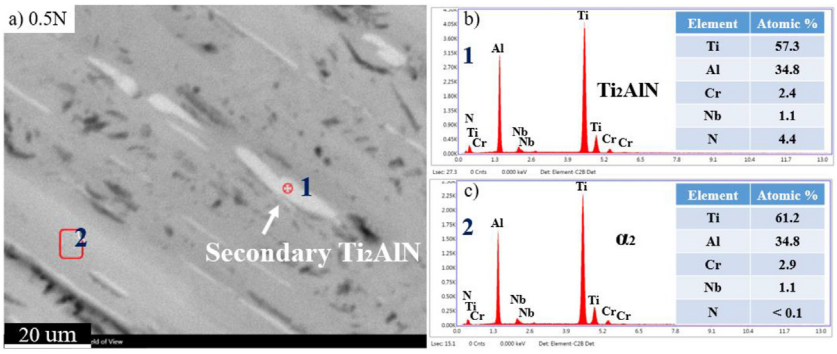

Fig. 12 – (a) SEM micrograph showing secondary Ti_2AlN precipitates in 0.5N HIPed alloy and (b and c) results of EDS analyses.

Alloy 1N: very fine, nearly fully lamellar dendritic features containing some primary Ti_2AlN precipitates
Alloy 2N: very much fine, nearly fully lamellar microstructure containing high amount of primary Ti_2AlN precipitates

The main microstructure in the 4822 alloy were coarse columnar fully lamellar dendrites and fine columnar lamellar dendrites, respectively (Fig. 6a). Increasing N content (0.5N alloy) resulted in nucleation of rare counts of primary Ti_2AlN precipitates and formation of equiaxed α dendrites due to changing the first solidified dendrites from β dendrites to α ones as shown in Fig. 6(c and d). Further increasing N content in the 1N (Fig. 6(e and f)) and 2N (Fig. 6(g and h) and 7 (g, h)) alloys, significantly increased the amount of primary Ti_2AlN precipitates which resulted in a significant microstructure refinement so that the colony size was reduced to 11 μm for the 2N alloy. Moreover, increasing N content caused formation of some α_2 or γ equiaxed grains and various shape of the primary Ti_2AlN precipitates (spherical, needle-like, shapeless and mostly rod-like) were formed in the 1N and 2N alloys. It is worth mentioning that in all as-cast alloys, lamellar microstructure was formed in the dendrites whereas the γ phase was formed in interdendritic regions.

In Fig. 7, the dark regions are interdendritic γ phase, and lighter regions are lamellar structure ($\alpha_2+\gamma$). In the 4822 alloy,

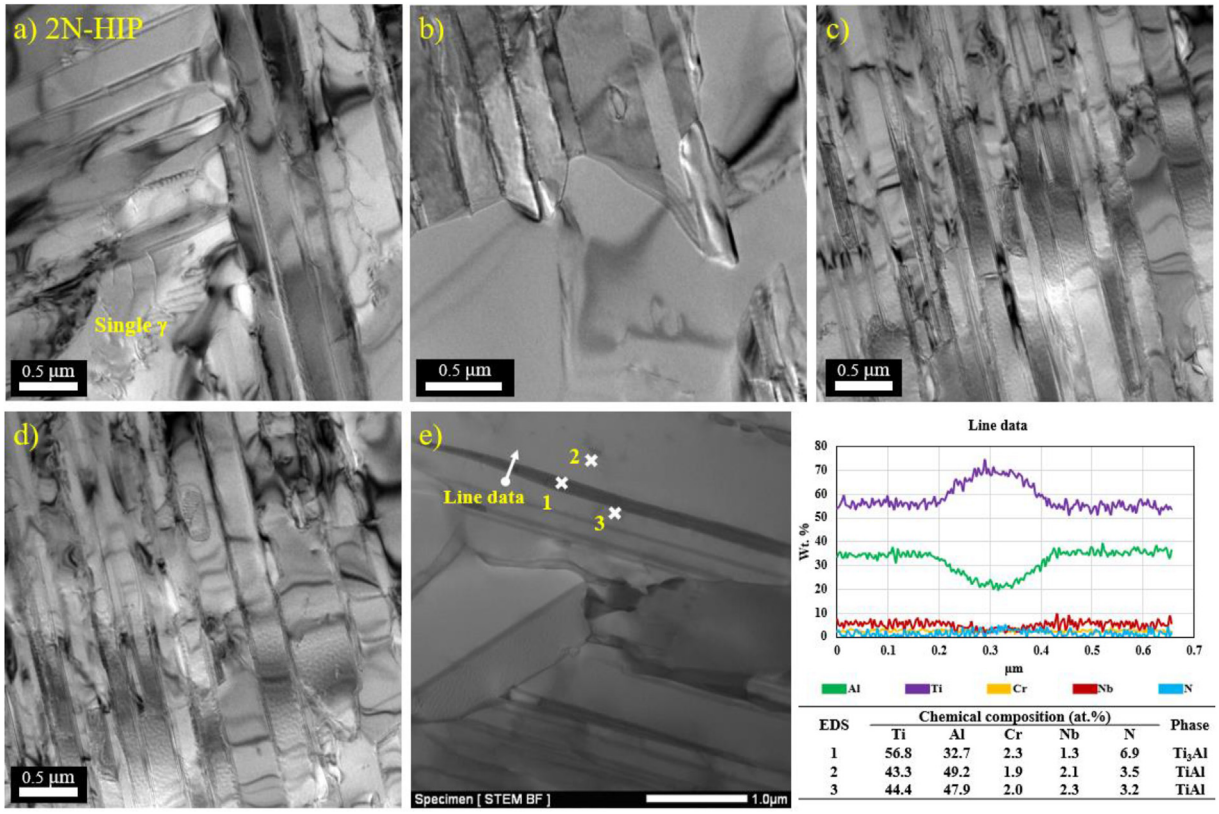

Fig. 13 – TEM/STEM micrographs of the nearly fully lamellar microstructure in the 2N–HIP alloy.

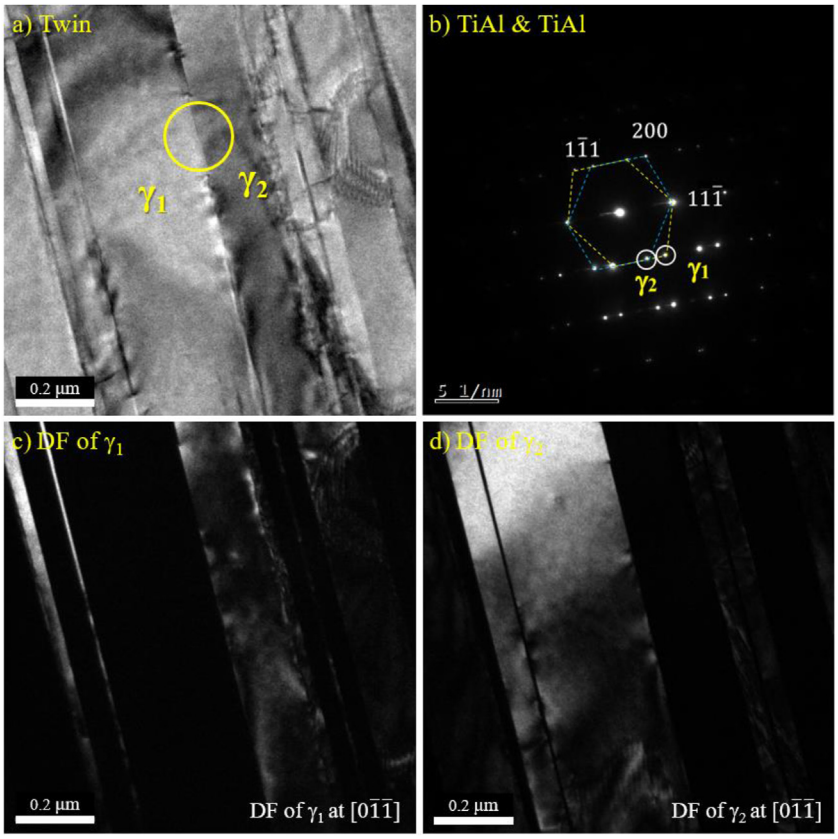

Fig. 14 – TEM micrographs with the corresponding SAD pattern of an annealing twin in the 2N–HIP alloy.

a white-colored network (Fig. 7a) can be identified in the core of dendrites being enriched in the Cr and Nb elements according to the EDS results (Fig. 8). This network is the remained β phase from the primary β phase dendrites which is also known as β phase segregation [11,18,21]. Therefore, it can be said that the β phase was the first solidified phase in the 4822 alloy. Interestingly, by increasing N content (0.5N alloy), the white-colored network was observed neither in the core of dendrites nor in the interdendritic regions due to the formation of primary α phase dendrites instead of β phase dendrites as shown in Fig. 7(c and d). Furthermore, there were few wire-shape phases (bright color) in the interdendritic region in the 0.5N alloy (instead of dendrite cores in the 4822 alloy); these bright color wire-shape phases were enriched in Cr, which suggests the formation of chromid precipitates or Cr segregation (Fig. 8e). Moreover, the volume fraction of precipitates decreased by increasing N content in the 1N (Fig. 7(c–f)) and 2N (Fig. 7h) alloys, respectively. The N addition and subsequent formation of the α phase dendrites instead of the β phase dendrites prevents the peritectic reaction, resulting in the reduction of the Cr and Nb segregation [17,20].

According to the literature, among all ternary Ti–Al–N nitride compounds (i.e., Ti_4AlN_3, Ti_3AlN and Ti_2AlN), Ti_2AlN is the most known and common ternary precipitate [10,13,17,18,20,34,37–39,45,47–49]. One should also note that Ti_4AlN_3 were not observed and detected in the form of precipitate in any related publications and also Ti_3AlN precipitates were only observable using HRTEM due to their nano-size [18,45,46,48,49]. The EDS analysis showed the precipitates formed in the studied alloys are composed of N, Al, and Ti. In addition, the Ti_2AlN is the most stable ternary compound according to the Thermo-Calc calculations reported in [33]. The results were also in accordance with XRD patterns in which the Ti_2AlN peaks were recognized. Consequently, the ternary nitride precipitates were identified as Ti_2AlN.

Considering the location of the primary Ti_2AlN precipitates, which were mostly located inside the lamellar colonies and rarely in the colony boundaries, significant refinement of microstructure, stability and high melting point of the primary Ti_2AlN precipitate and Thermo-Calc^R calculations reported in [33], it can be said that primary Ti_2AlN precipitates were the first solidified phases in the N-bearing alloys, acting as nucleation sites for dendrites of the α phase and also preventing coarsening of the dendritic structure [10,17,18,20,46].

3.2.4. *Nucleation mechanism of primary Ti_2AlN precipitates*

Recently, Tan et al. [39] reported a mechanism for nucleation of Ti_2AlN phase during solidification of the $Ti_{46}Al_4Nb_1Mo$-xN (x = 0.4, 0.8, 1.2, 1.6 at.%) alloys. They suggested that reproduced TiN and γ(TiAl) phases are the first solidified phases and then Ti_2AlN nucleates via the reaction of TiAl and TiN phases. The authors believe that their proposed mechanism may not be correct due to several reasons. Firstly, the $Ti_{46}Al$ alloy is solidified through β phase based on the Ti–Al binary

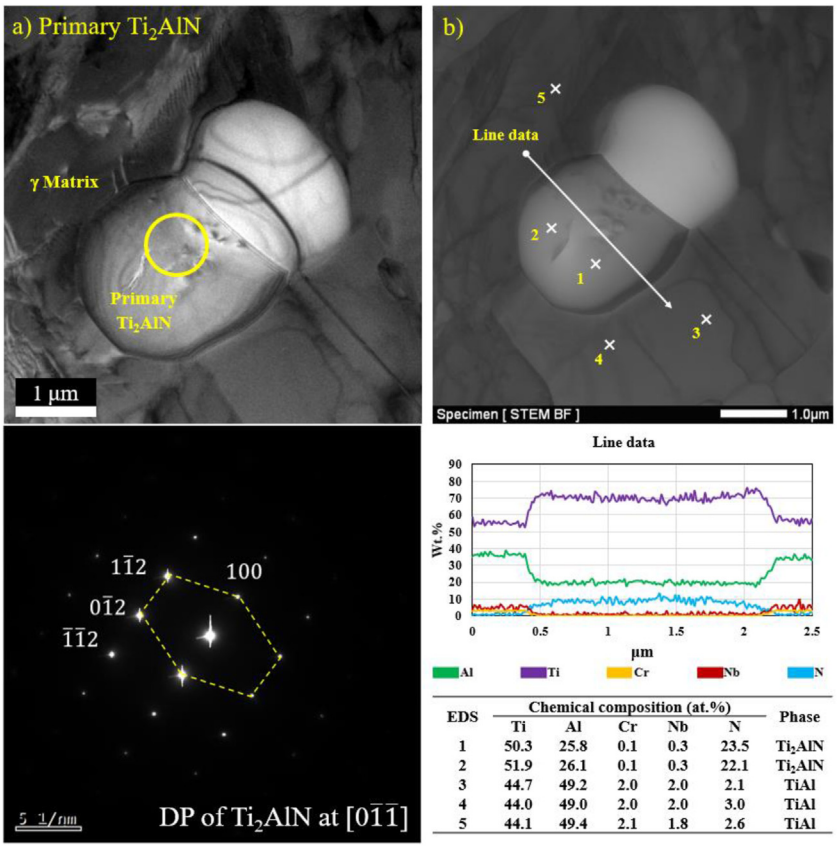

EDS	Chemical composition (at.%)					Phase
	Ti	Al	Cr	Nb	N	
1	50.3	25.8	0.1	0.3	23.5	Ti_2AlN
2	51.9	26.1	0.1	0.3	22.1	Ti_2AlN
3	44.7	49.2	2.0	2.0	2.1	TiAl
4	44.0	49.0	2.0	2.0	3.0	TiAl
5	44.1	49.4	2.1	1.8	2.6	TiAl

Fig. 15 – TEM/STEM micrographs with the corresponding SAD pattern and EDS of the primary Ti_2AlN precipitate in the 2N–HIP alloy.

phase diagram. Furthermore, Nb [50] and N [10] are α stabilizing elements while Mo stabilizes β phase. Thus, $Ti_{46}Al_4Nb_1Mo$-xN alloys could not be solidified through γ(TiAl) phase, and γ could not be among the first solidified phases. Moreover, based on the approximate melting points of the TiN (higher than 3000 °C), TiAl (lower than 1500 °C) and Ti_2AlN (2500 °C [51]), TiAl could not be formed earlier than Ti_2AlN. Finally, if the TiAl phase was able to be formed earlier than the Ti_2AlN one, it would significantly have impeded the nucleation effects of the Ti_2AlN precipitates while the resultant microstructures in [39] were considerably refined.

Fig. 9 shows a possible mechanism for nucleation of primary Ti_2AlN precipitates suggested by the present authors. To fabricate N-bearing alloys, TiN powder was used. TiN has a very high melting point (higher than 3000 °C). So it is not melted in the VAR furnace (as explained in section 2), and it should be dissolved in the melt. Atomic bonds in TiN tend to be more ionic than covalent bonds [50,51]; therefore, TiN is dissolved in the melt via releasing Ti and N ions (TiN → Ti + N) instead of releasing TiN molecules. Therefore, based on the N content of the alloys (amount of added TiN powders), the following behaviors are expected.

1) N with a lower content than its solubility limit (i.e., 0.5N alloy or 0.4 at. % N alloy in [39]): As can be seen from Fig. 9(a–d), the TiN particles are dissolved completely, and no primary Ti_2AlN precipitate is formed.
2) N with a higher content than its solubility limit (i.e., 1N alloy): As can be seen from Fig. 9(e–i), the TiN particles are dissolved until the N content of the melt reaches its solubility limit. Then, Ti_2AlN is nucleated on the surface of undissolved TiN particles via a reaction of Ti and Al with TiN particles' surfaces, TiN + Al + Ti → Ti_2AlN and 2TiN + Al → Ti_2AlN + N (Fig. 9h). Due to the turbulent melt, the primary Ti_2AlN precipitates are separated and dispersed in various shapes providing nucleation sites in the melt (Fig. 9i), and finally, TiN powders will wholly be transformed.
3) N with a much higher content than its solubility limit (i.e., 2N alloy): As can be seen from Fig. 9(e–i), the formation of high amount of the Ti_2AlN precipitates in the melt reduces the TiN to Ti_2AlN transformation rate, and finally, few undissolved TiN powder particles or Ti_2AlN with TiN core particles stay in the melt (Fig. 9n). The rare undissolved TiN particles were ignored similar to other studies.

It is worth mentioning that in the present work, various ways were tried to completely transform TiN powders to Ti_2AlN precipitates during re-melting of the 2N alloy, such as increasing melting time and electric current intensity to about 550A, but none of them did work. Thanks to these experiments, it was found that the vacuum level of VAR furnace significantly affects the formation and dissolution of both TiN and Ti_2AlN phases by controlling the direction of the TiN to

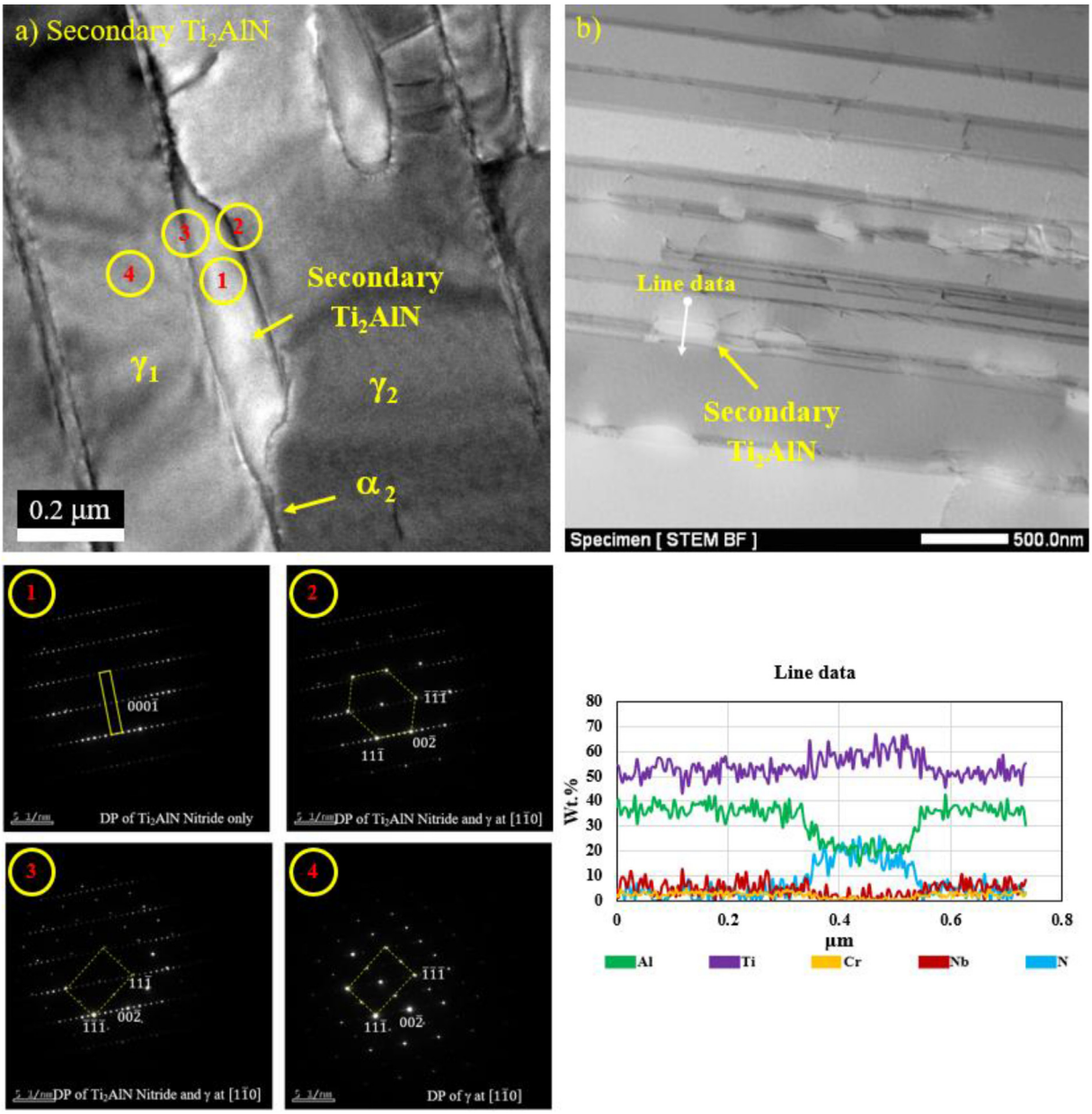

Fig. 16 – TEM/STEM micrographs with the corresponding SAD patterns and EDS of the secondary Ti_2AlN precipitate in the 2N–HIP alloy.

Ti_2AlN transformation ($2TiN + Al \rightarrow Ti_2AlN + N$), as different fractions of remained TiN and Ti_2AlN phases and Ti_2AlN with TiN core particles were found in the samples re-melted under different vacuum levels [30,31]. Interestingly, it is possible to produce titanium aluminide composites reinforced by the Ti_2AlN with TiN core particles by controlling the atmosphere of VAR furnace [31,32].

3.3. *The HIPed intermetallic alloys*

3.3.1. *Phase analysis*

Fig. 10 shows XRD patterns indicating the existence of both α_2 and γ phases in all the HIPed alloys. Moreover, the formation of Ti_2AlN phase in the 1N–HIP and 2N–HIP alloys was confirmed. In the 4822 alloy, the intensity of the common peak of α_2 and γ phases decreased after the HIP treatment in spite of increasing the intensity of γ phase peak. Unlike the as-cast 1N alloy, the formation of Ti_2AlN phase in the 1N–HIP was also confirmed. Furthermore, new Ti_2AlN peaks were detected in the 2N–HIP alloy.

3.3.2. *Microstructures*

Fig. 11 shows optical and SEM micrographs of the HIPed alloys. The microstructure of the 4822-HIP alloy is mainly duplex and only a small volume fraction of the dendritic structure from solidification stage has remained. However, the microstructure of the 0.5N–HIP alloy is a mixture of dendritic structure and duplex. This is consistent with the XRD patterns as the

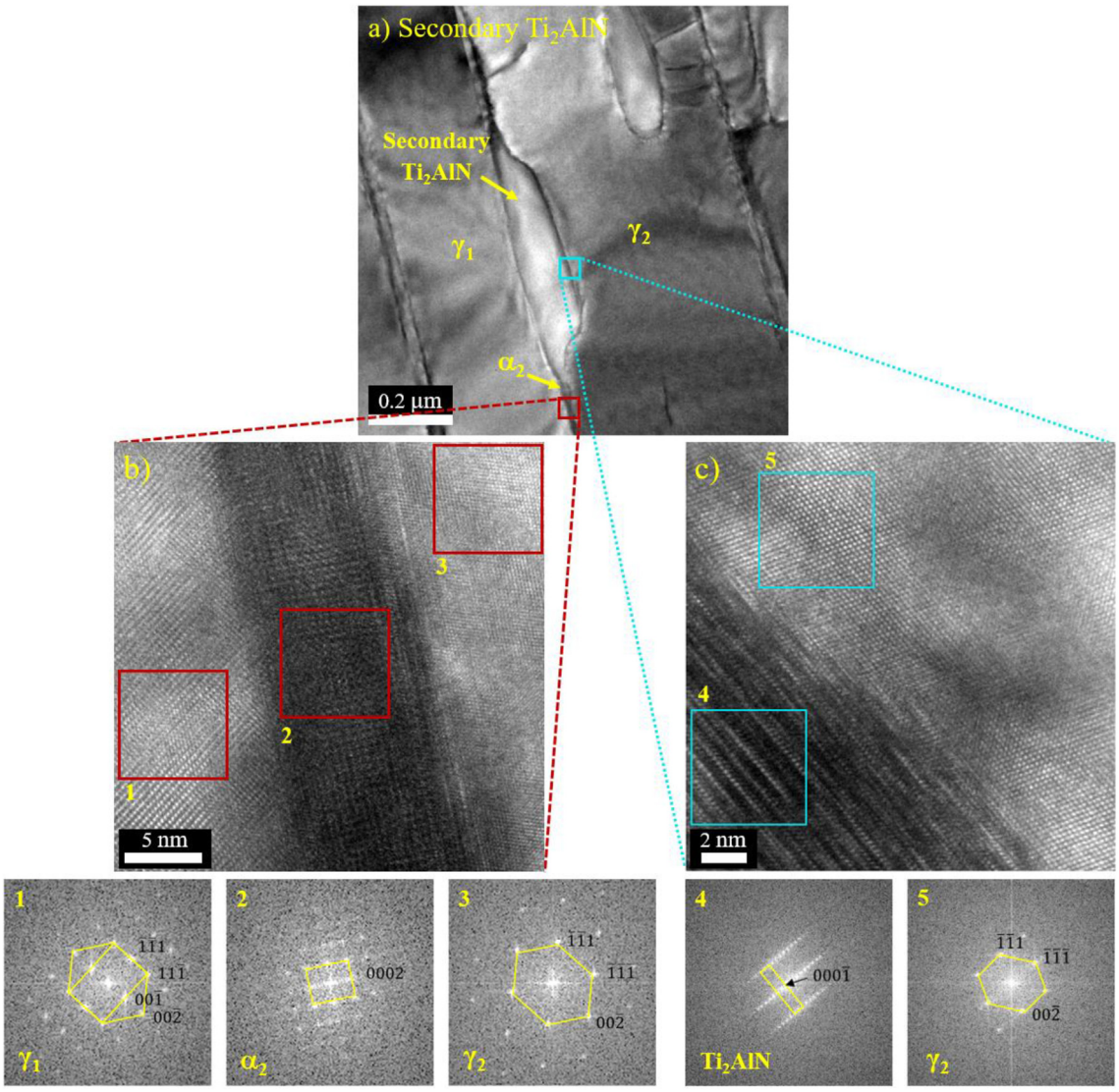

Fig. 17 – a) TEM micrograph of the secondary Ti_2AlN precipitate, HRTEM micrographs with the corresponding FFT patterns of b) $\gamma+\alpha_2+\gamma$ lamellas, and c) Ti_2AlN and γ lamella.

intensity of γ phase peak for the 4822-HIP alloy is higher compared to the 0.5N–HIP one (Fig. 10). The duplex microstructure fraction of the 1N–HIP alloy was negligible (Fig. 11e), and the nearly fully lamellar microstructure of 2N–HIP alloy was maintained after HIP treatment. Therefore, increasing N content resulted in lower duplex structure fraction. This may lead to a higher microstructure stability due to impeding effect of N on diffusion of atoms and its locking effect [52]. For instance, N addition up to 1 at.% to Ti–48Al-1.5Mo changed the time of duplex structure transformation from 2 h to 24 h at 1300 °C and achieving the duplex microstructure by heat treating at lower than 1300 °C required time more than 48 h [52]. As shown in Fig. 11(b, d, f), the remained β phase and Cr segregation were completely dissolved after HIP operation, and the white-colored network of β phase and bright Cr-rich phases were no longer observed in the HIPed alloys. In addition, comparing HIPed samples with as-cast ones reveals no obvious changes in size and fraction of primary Ti_2AlN precipitates in the HIPed 0.5N, 1N, and 2N alloy. It should be mentioned that the primary titanium nitrides were identified based on some features such as their morphology, size, location, EDS analysis and XRD patterns. The primary Ti_2AlN with different morphologies of spherical, needle-like, shapeless and mostly rod-like are usually located within the lamellar colonies and are larger than the secondary Ti_2AlN precipitates. However, as shown in Fig. 11(d, f, h), many new secondary nitride precipitates were formed in the HIPed 0.5N, 1N, and 2N alloys, which were uniformly distributed at all interfaces of $(\alpha_2+\gamma)$ lamellas. Meanwhile, they became more linear in the 1N–HIP and 2N–HIP alloys. Based on the increase in Ti_2AlN peaks in the XRD patterns (Fig. 10), microstructural observations using OM and SEM (Fig. 11) and EDS analysis (Fig. 12), it can be confirmed that the new nitride precipitates are secondary Ti_2AlN precipitates. Our previous study [33] showed that secondary Ti_2AlN precipitates are dissolved during high-temperature heat treatments, and their nucleation and growth can be

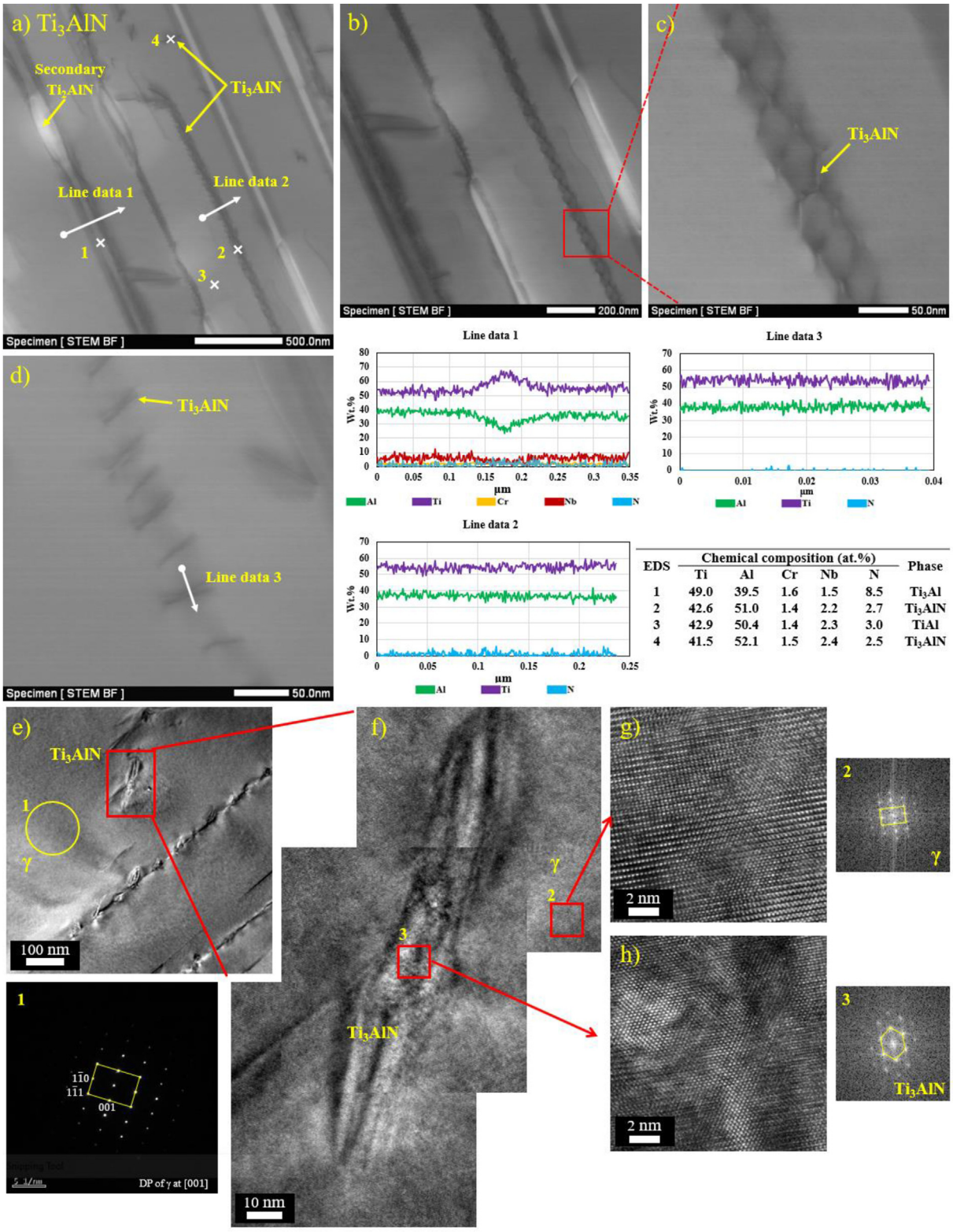

Fig. 18 – STEM/TEM/HRTEM micrographs with the corresponding SAD and FFT patterns and with EDS of the nano-sized Ti_3AlN precipitate in the 2N–HIP alloy.

controlled by adjusting the cooling rate. For instance, the precipitates were formed again during furnace cooling after dissolving at 1400 °C, while air cooling prevented their re-precipitation. Another type of secondary nitride precipitates was also identified in the HIPed alloys was a nano-sized Ti_3AlN precipitate which will be discussed in details later.

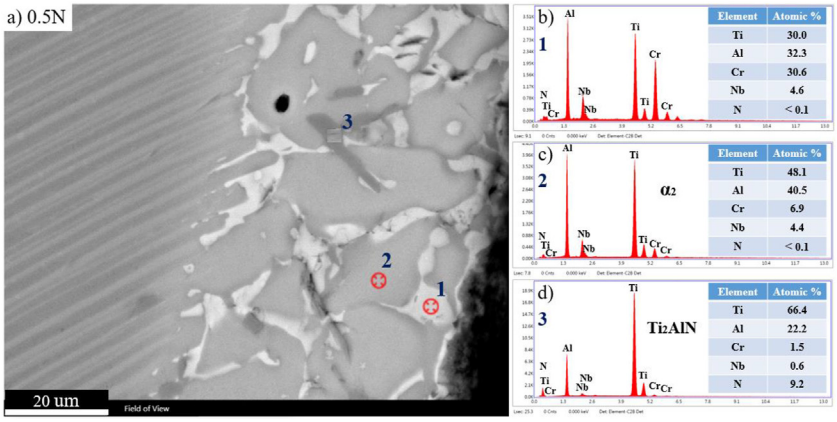

Fig. 19 – (a) SEM image of the white layer in the 0.5N HIPed alloy (b–d) results of the EDS analyses.

Figs. 13 and 14 show TEM/STEM results of the nearly fully lamellar structure of the 2N–HIP alloy. The average thickness of the α_2 and γ lamellas was 0.04 ± 0.01 μm and 0.24 ± 0.12 μm, respectively, Thus, α_2 and γ lamellas are extremely fine, which can be good for mechanical properties. TEM images with the corresponding SAD pattern of a γ/γ interface are shown in Fig. 14 where the orientation relationship (OR) $(1\bar{1}1)_{\gamma 1} \parallel (1\bar{1}1)_{\gamma 2}$// $[01\bar{1}]_{\gamma 1} \parallel [01\bar{1}]_{\gamma 2}$ is detected. Such OR is similar to what is usually observed in annealing twin boundary of FCC materials. It can be expected that by further dissolution of the α_2 phase, the two adjacent γ phases will achieve such OR. Twins, especially mechanical nano-twins, significantly improve mechanical properties as in the work by Chen et al. [53].

Fig. 15 shows TEM/STEM images with the corresponding SAD pattern of one of the incoherent primary nitride precipitates in the 2N–HIP alloy. Based on the results, the precipitates are the Ti_2AlN phase. Figs. 16 and 17 also show TEM/STEM/HRTEM images with the corresponding SAD and FFT patterns and EDS of a secondary Ti_2AlN precipitate and its neighbor lamellas in the 2N–HIP alloy. Overlap of all γ-TiAl diffraction spots with {0001} family planes of the Ti_2AlN precipitate at both sides can be clearly seen. Therefore, the fully coherent nature of the particle at this inter-lamellar position is clarified. Fig. 17b shows that the black-burn OR still exists between γ and α_2 lamellas and the N addition up to 2 at.% did not change this OR. Fig. 17c shows that at the interface between the γ lamella and the secondary Ti_2AlN precipitate, we can also witness coherency caused by OR existing between these two phases. At the interface between the secondary Ti_2AlN precipitate and the γ lamella, the $(\bar{1}11)$ of the γ phase is parallel with the (0001) plane family of Ti_2AlN. Therefore, it is deduced that by decomposition of α_2 lamella and growth of γ lamella, secondary Ti_2AlN precipitates are formed in the former α_2 regions, and a thin lamella of α_2 has remained. Also, a twin-like phase boundary is formed in some areas where two lamellas come into contact with each other.

Fig. 18 shows STEM/TEM/HRTEM micrographs with the corresponding SAD and FFT patterns with EDS of the nano-sized Ti_3AlN precipitates in the 2N–HIP alloy. The precipitates formed inside the single γ phase and also at the interfaces of $(\gamma+\alpha_2)$ lamellas had a width and length of about 2–6 nm and 30–40 nm, respectively. Based on the EDS point results, the N content of the matrix is much higher than the solubility limit of N in both γ and α_2 phases (<0.1 for γ, and 0.7–1.4 for α_2 [10]), showing that they are still supersaturated with N atoms. Considering the nano-size of the Ti_3AlN precipitates and high N content in the matrix, one can conclude that thermal history during HIP was not sufficient enough to release N atoms, and thus the precipitates experienced the earlier stage of their growth. Fig. 18(a–c) show beautiful chains of the nano-sized Ti_3AlN precipitates. Although the formation mechanism of the chains is not clear, they were probably formed by consuming the α_2 lamella. Also, the existence of nano-sized Ti_3AlN precipitates inside single γ lamella (Fig. 18d) indicates that the precipitates can also be formed as a result of the γ phase consumption.

Fig. 19a shows a layered microstructure formed on the surface of the buttons, which is called white layer. The white layer being enriched in Cr and Nb was formed following the HIP operation and contained Cr and Nb-rich precipitates, Ti_2AlN precipitates, and α_2 phase matrix. The color phases in Fig. 19 is different from Figs. 11 and 15 due to the heavy elements of the matrix. For example, the Ti_2AlN precipitates can be identified with the dark gray color in Fig. 19a and with the white color in Figs. 11 and 15. The thickness of the white layer in N-bearing alloys was much thinner than that for the 4822-HIP alloy due to impeding effect of N on the diffusion of elements.

4. Conclusions

In this research, different Ti–48Al–2Cr–2Nb-xN (x = 0, 0.5, 1 and 2 at.%) alloys were fabricated via the vacuum arc re-melting method and solidification behavior and microstructural features of the as-cast and HIPed samples were investigated. Some of the main results are as follows.

1) N addition changed solidification path from the primary β phase to the α phase.
2) N addition significantly decreased colony size to 11 μm in the 2N alloy and refined dendritic structure.

3) N addition increased microstructure uniformity of the N-bearing alloys compared to the base 4822 alloy.
4) N addition higher than the solubility limit (near 0.5 at.% N) led to the formation of primary Ti_2AlN precipitates. The precipitates were almost located within the lamellar colonies following solidification.
5) After the HIP operation, dendritic structure of the 4822 alloy was broken and turned to a more uniform duplex microstructure. However, N addition resulted in much more microstructure stability such that the 2N alloy was the most stable one following the HIP operation.
6) After the HIP operation, a highly extended network of secondary Ti_2AlN precipitates was formed at α_2/γ interfaces in the N-bearing alloys, even in 0.5N– HIP alloy with a very low volume fraction of primary Ti_2AlN precipitates.
7) Nano-sized Ti_3AlN precipitates were formed in the 2N–HIP alloy.

Declaration of Competing Interest

The authors declare that they have no known competing financial interests or personal relationships that could have appeared to influence the work reported in this paper.

Acknowledgements

The financial support from the Iran National Science Foundation (research project no. 98006118) is gratefully acknowledged.

REFERENCES

[1] Bewlay BP, Nag S, Suzuki A, Weimer MJ. TiAl alloys in commercial aircraft engines. Mater High Temp 2016;33:549–59. https://doi.org/10.1080/09603409.2016.1183068.
[2] Kothari K, Radhakrishnan R, Wereley NM. Advances in gamma titanium aluminides and their manufacturing techniques. Prog Aero Sci 2012;55:1–16. https://doi.org/10.1016/j.paerosci.2012.04.001.
[3] Appel F, Paul JDH, Oehring M. Gamma titanium aluminide alloys: science and technology. John Wiley & Sons; 2011. https://books.google.com/books?id=M-4lNNJsyF8C.
[4] Clemens H, Mayer S. Design, processing, microstructure, properties, and applications of advanced intermetallic TiAl alloys. Adv Eng Mater 2013;15:191–215. https://doi.org/10.1002/adem.201200231.
[5] Zhang C, Zhang Sh, Pan Y, Xu W, Singh H-P, Liu B, et al. Effect of Sn addition on the mechanical properties and high-temperature oxidation resistance of intermetallic TiAl alloys by first principles study and experimental investigation. J Mater Res Technol 2022;21:3666–77. https://doi.org/10.1016/j.jmrt.2022.11.007.
[6] Hu D. Role of boron in TiAl alloy development: a review. Rare Met 2016;35:1–14. https://doi.org/10.1007/s12598-015-0615-1.
[7] Kawabata T, Tadano M, Izumi O. Effect of carbon and nitrogen on mechanical properties of TiAl alloys. ISIJ Int 1991;31:1161–7. https://doi.org/10.2355/isijinternational.31.1161.
[8] Klein T, Schachermayer M, Mendez-Martin F, Schöberl T, Rashkova B, Clemens H, et al. Carbon distribution in multi-phase $γ$-TiAl based alloys and its influence on mechanical properties and phase formation. Acta Mater 2015;94:205–13. https://doi.org/10.1016/j.actamat.2015.04.055.
[9] Lapin J, Štamborská M, Kamyshnykova K, Pelachová T, Klimová A, Bajana O. Room temperature mechanical behaviour of cast in-situ TiAl matrix composite reinforced with carbide particles. Intermetallics 2019;105:113–23. https://doi.org/10.1016/j.intermet.2018.11.007.
[10] Zhang T, Wu Z, Hu R, Zhang F, Kou H, Li J. Influence of nitrogen on the microstructure and solidification behavior of high Nb containing TiAl alloys. Mater Des 2016;103:100–5. https://doi.org/10.1016/j.matdes.2016.04.071.
[11] Wang D, Sun D, Han X, Wang Q. In situ Ti2AlN reinforced TiAl-based composite with a novel network structure: microstructure and flexural property at elevated temperatures. Mater Sci Eng A 2019;742:231–40. https://doi.org/10.1016/j.msea.2018.11.018.
[12] Saeedipour S, Kermanpur A. On the microstructure and solidification behavior of N-bearing Ti-46Al-8Ta (at.%) intermetallic alloys. J Mater Eng Perform 2019;28:6438–48. https://doi.org/10.1007/s11665-019-04372-w.
[13] Saeedipour S, Kermanpur A, Sadeghi F. Effect of N addition on microstructure refinement and high temperature mechanical properties of Ti–46Al–8Ta (at. %) intermetallic alloy. J Alloys Compd 2020;817:152749. https://doi.org/10.1016/j.jallcom.2019.152749.
[14] Ahmadi Siahboumi A, Kermanpur A, Ghorbani HR, Belova L. Effect of hafnium addition on microstructure and room temperature mechanical properties of the Ti-48Al-2Cr-2Nb intermetallic alloy. J Alloys Compd 2022;917:165467. https://doi.org/10.1016/j.jallcom.2022.165467.
[15] Klein T, Usategui L, Rashkova B, Nó ML, San Juan J, Clemens H, et al. Mechanical behavior and related microstructural aspects of a nano-lamellar TiAl alloy at elevated temperatures. Acta Mater 2017;128:440–50. https://doi.org/10.1016/j.actamat.2017.02.050.
[16] Guyon J, Hazotte A, Wagner F, Bouzy E. Recrystallization of coherent nanolamellar structures in Ti48Al2Cr2Nb intermetallic alloy. Acta Mater 2016;103:672–80. https://doi.org/10.1016/j.actamat.2015.10.049.
[17] Liu Y, Hu R, Yang J, Li J. Tensile properties and fracture behavior of in-situ synthesized Ti2AlN/Ti48Al2Cr2Nb composites at room and elevated temperatures. Mater Sci Eng A 2017;679:7–13. https://doi.org/10.1016/j.msea.2016.09.105.
[18] Liu Y, Hu R, Zhang T. Microstructure stability of Ti2AlN/Ti–48Al–2Cr–2Nb composite at 900 °C. Trans Nonferrous Metals Soc China 2016;26:423–30. https://doi.org/10.1016/S1003-6326(16)64095-5.
[19] Wang D, Sun D, Han X, Wang Q, Zhang N, Xu F. Fabrication and mechanical properties of in situ synthesized Ti2AlN/TiAl composite. J Mater Eng Perform 2018;27:4336–44. https://doi.org/10.1007/s11665-018-3517-1.
[20] Liu Y, Hu R, Zhang T, Kou H, Li J. Microstructure characterization and mechanical properties of in situ synthesized Ti2AlN/Ti48Al2Cr2Nb composites. Adv Eng Mater 2014;16:507–10. https://doi.org/10.1002/adem.201300417.
[21] Liu P, Han X, Sun D, Wang Q. First-principles investigation on the structures, energies, electronic and defective properties of Ti2AlN surfaces. Appl Surf Sci 2018;433:1056–66. https://doi.org/10.1016/j.apsusc.2017.10.112.

[22] Liu P, Han X, Sun D, Chen Z, Wang Q. Adhesion, stability and electronic properties of Ti2AlN(0001)/TiAl(111) coherent interface from first-principles calculation. Intermetallics 2018;96:49–57. https://doi.org/10.1016/j.intermet.2018.02.012.
[23] Liu P, Han X, Sun D, Wang Q. Development and application of a ternary Ti-Al-N interatomic potential for Ti2AlN/TiAl composite. J Alloys Compd 2018;745:63–74. https://doi.org/10.1016/j.jallcom.2018.02.168.
[24] Han X, Liu P, Sun D, Wang Q. Quantifying the role of interface atomic structure in the compressive response of Ti2AlN/TiAl composite using MD simulations. J Mater Sci 2019;54:5536–50. https://doi.org/10.1007/s10853-018-03237-2.
[25] Han X, Liu P, Sun D, Wang Q. Molecular dynamics simulations of the tensile responses and fracture mechanisms of Ti2AlN/TiAl composite. Theor Appl Fract Mech 2019;101:217–23. https://doi.org/10.1016/j.tafmec.2019.03.003.
[26] Liu P, Han X, Sun D, Wang Q. The effect of interface atomic structure on the deformation mechanisms of Ti2AlN/TiAl composite under nanoindentation using MD simulations. J Phys Condens Matter 2019;31:125002. https://doi.org/10.1088/1361-648x/aafd0e.
[27] Han X, Liu P, Sun D, Wang Q. The role of incoherent interface in evading strength-ductility trade-off dilemma of Ti2AlN/TiAl composite: a combined in-situ TEM and atomistic simulations. Compos B Eng 2020;185:107794. https://doi.org/10.1016/j.compositesb.2020.107794.
[28] Zhang Y, Franke P, Seifert HJ. CALPHAD modeling of metastable phases and ternary compounds in Ti-Al-N system. Calphad 2017;59:142–53. https://doi.org/10.1016/j.calphad.2017.09.006.
[29] Zhou Y, Sun D-L, Jiang D-P, Han X-L, Wang Q, Wu G-H. Microstructural characteristics and evolution of Ti2AlN/TiAl composites with a network reinforcement architecture during reaction hot pressing process. Mater Char 2013;80:28–35. https://doi.org/10.1016/j.matchar.2013.03.007.
[30] Ghorbani HR, Kermanpur A, Rezaeian A. Evaluating effect of nitrogen addition on Ti-48Al-2Cr-2Nb (at. %) alloy and effective factors on the presence of titanium nitride in the microstructure of nitrogen-containing alloy. In: 3rd Natl. Conf. Mater. Metall. Min. Eng. Ahwaz, Iran: Shahid Chamran university; 2020. https://www.civilica.com/Paper-MCONF03-MCONF03_060.html.
[31] Ghorbani HR, Kermanpur A, Rezaeian A. Manufacturing and characterization of a novel titanium aluminide composite with Ti2AlN reinforcing particles with TiN core. In: Second Natl. Conf. Comput. Exp. Mech. Tehran, Iran: Shahid Rajaee Teacher Training University; 2020. https://www.civilica.com/Paper-CEMCONF02-CEMCONF02_050.html.
[32] Ghorbani HR, Kermanpur A, Rezaeian A. Investigating interaction of cracks and particles in a titanium aluminide composite with Ti2AlN reinforcing particles with TiN core. In: Second Natl. Conf. Comput. Exp. Mech. Tehran, Iran: Shahid Rajaee Teacher Training University; 2020. https://www.civilica.com/Paper-CEMCONF02-CEMCONF02_028.html.
[33] Ghorbani HR, Kermanpur A, Rezaeian A, Ahmadi Siahboumi A, Ali Taebi M. Effect of N addition on microstructure and high temperature mechanical properties of Ti-48Al-2Cr-2Nb (at. %) intermetallic alloy. Mater Today Commun 2020;25:101494. https://doi.org/10.1016/j.mtcomm.2020.101494.
[34] Liu P, Sun D, Han X, Wang Q. Investigation on the crystallographic orientation relationships and interface atomic structures in an in-situ Ti2AlN/TiAl composite. Mater Des 2017;130:239–49. https://doi.org/10.1016/j.matdes.2017.05.061.
[35] Ghorbani HR, Kermanpur A, Rezaeian A, Sadeghi F, Ahmadi Siahboumi A. Effect of nitrogen addition and aging treatment on microstructure and high temperature mechanical properties of Ti-48Al-2Cr-2Nb (at%) intermetallic alloy. J Alloys Compd 2022;904:164077. https://doi.org/10.1016/j.jallcom.2022.164077.
[36] Nam CY, Oh MH, Kumar KS, Wee DM. Effect of nitrogen on the mean lamellar thickness of fully lamellar TiAl alloys. Scripta Mater 2002;46:441–6. https://doi.org/10.1016/S1359-6462(02)00011-8.
[37] Nam CY, Wee DM, Wang P, Kumar KS. Microstructure and toughness of nitrogen-doped TiAl alloys. Intermetallics 2002;10:113–27. https://doi.org/10.1016/S0966-9795(01)00116-9.
[38] Tan Y, Chen R, Liu Y, Ding H, Su Y, Guo J, et al. Formation of Ti2AlN and TiB and its effect on mechanical properties of Ti46Al4Nb1Mo alloy by adding BN particles. Mater Sci Eng A 2019;756:161–71. https://doi.org/10.1016/j.msea.2019.04.046.
[39] Tan Y, Fang H, Cui H, Liu Y, Chen R, Su Y, et al. Room and high temperature mechanical behavior of Ti–Al–Nb–Mo alloy reinforced with Ti2AlN ceramic particles. Mater Sci Eng A 2020;797:140098. https://doi.org/10.1016/j.msea.2020.140098.
[40] ASTM Standard Procedure E1508-12a(2019). Standard guide for quantitative analysis by energy-dispersive spectroscopy. https://www.astm.org/e1508-12ar19.html; 2019.
[41] Siahboumi AA, Kermanpur A, Sadeghi F, Ghorbani HR. Effect of Hf addition on solidification and hot isostatically pressed microstructures of the Ti-48Al-2Cr-2Nb (at%) intermetallic alloy. J Alloys Compd 2021;860:158437. https://doi.org/10.1016/j.jallcom.2020.158437.
[42] McCullough C, Valencia JJ, Levi CG, Mehrabian R. Peritectic solidification of TiAlTa alloys in the region of γ-TiAl. Mater Sci Eng A 1992;156:153–66. https://doi.org/10.1016/0921-5093(92)90147-S.
[43] McCullough C, Valencia JJ, Levi CG, Mehrabian R. Phase equilibria and solidification in Ti-Al alloys. Acta Metall 1989;37:1321–36. https://doi.org/10.1016/0001-6160(89)90162-4.
[44] Zhong H, Li S, Kou H, Li J. The solidification path related columnar-to-equiaxed transition in Ti–Al alloys. Intermetallics 2015;59:81–6. https://doi.org/10.1016/j.intermet.2014.12.014.
[45] Sujata M, Sastry DH, Ramachandra C. Microstructural characterization and creep behaviour of as-cast titanium aluminide Ti–48Al–2V. Intermetallics 2004;12:691–7. https://doi.org/10.1016/j.intermet.2004.02.007.
[46] Liu Y, Hu R, Zhang T, Kou H, Li J. Microstructure evolution and nitrides precipitation in in-situ Ti2AlN/TiAl composites during isothermal aging at 900 °C. Trans Nonferrous Metals Soc China 2014;24:1372–8. https://doi.org/10.1016/S1003-6326(14)63201-5.
[47] Tian WH, Nemoto M. Precipitation behavior of nitrides in L10-ordered TiAl. Intermetallics 2005;13:1030–7. https://doi.org/10.1016/j.intermet.2004.09.014.
[48] Cho HS, Nam SW, Yun JH, Wee DM. Effect of 1 at.% nitrogen addition on the creep resistance of two phase TiAl alloy. Mater Sci Eng A 1999;262:129–36. https://doi.org/10.1016/S0921-5093(98)00996-4.
[49] Sun D, Sun T, Wang Q, Han X, Guo Q, Wu G. Fabrication of in situ Ti2AlN/TiAl composites by reaction hot pressing and their properties. J Wuhan Univ Technol Sci Ed 2014;29:126–30. https://doi.org/10.1007/s11595-014-0879-6.

[50] Lapin J. TiAl-based alloys: present status and future perspectives. In: Conf. Proc. Met.; 2009. p. 2009.
[51] Choi E-S, Sung J, Wang Q, Kim K-H, Busnaina A, Kang MC. Material properties and machining performance of hybrid Ti2AlN bulk material for micro electrical discharge machining. Trans Nonferrous Metals Soc China 2012;22:s781–6. https://doi.org/10.1016/S1003-6326(12)61804-4.
[52] Yun JH, Wee DM, Oh MH, Inui H, Yamaguchi M. Nitrogen-doped TiAl alloys Part I Microstructure control. J Mater Sci 2000;35:4527–32. https://doi.org/10.1023/A:1004860419517.
[53] Chen G, Peng Y, Zheng G, Qi Z, Wang M, Yu H, et al. Polysynthetic twinned TiAl single crystals for high-temperature applications. Nat Mater 2016;15:876–81. https://doi.org/10.1038/nmat4677.